NKS-464
ISBN 978-87-7893-557-1

Micromechanical modeling of single crystal and polycrystalline UO_2 at elevated temperatures

Matti Lindroos[1]
Napat Vajragupta[1]
Janne Heikinheimo[1]
Diogo Ribeiro Costa[2]
Abhishek Biswas[1]
Tom Andersson[1]
Pär Olsson[2]

[1]VTT Technical Research Centre of Finland Ltd
[2]KTH Royal Institute of Technology, Sweden

November 2022

Abstract

Understanding cracking phenomena in polycrystalline UO_2 fuel pellet requires detailed knowledge of the fuel's local microscopic stresses and operational conditions. High stress states emerge in the pellet due to a deep parabolic temperature gradient between the center and cylindrical edges of the pellet. In normal operating conditions, the outer regions of the fuel pellet are brittle and experience tensile stresses. On the other hand, the inner parts of the pellet experience compressive stresses, and the behavior is increasingly plastic. Macroscopic stress in the pellet can cause diverging local stresses and microcracking due to e.g. strain incompatibilities between the grains and dislocation pile-ups. Also, porosity, localization of pores in grains and at grain boundaries, their size, and shape substantially impact UO_2 cracking behavior.

This study proposes a micromechanical modeling workflow to study how pores affect the plasticity of polycrystalline UO_2. SEM-EBSD was performed on standard UO_2 pellets with dense microstructure and round pores at inter and intra-granular locations. The characterized microstructure was meshed and coupled with a dislocation-based crystal plasticity model to simulate the uniaxial compression behavior at 1600 K. To this end, we propose the constitutive model that potentially can describe the deformation of a single crystal and polycrystalline UO_2. We have also developed the inverse optimization method to identify material parameters providing a unique solution at different length scales. With the element removal technique, we have assessed the influence of pores size, volume fraction, and their distribution in microstructures on the mechanical response of polycrystalline UO_2.

Key words

Crystal plasticity, Uranium dioxide, Mechanical behavior,
Porosity, Strain localization, SEM-EBSD

NKS-464
ISBN 978-87-7893-557-1
Electronic report, November 2022
NKS Secretariat
P.O. Box 49
DK - 4000 Roskilde, Denmark
Phone +45 4677 4041
www.nks.org
e-mail nks@nks.org

Micromechanical modeling of single crystal and polycrystalline UO_2 at elevated temperatures

Final Report from the NKS-R POMMI activity (Contract: AFT/NKS-R(21)131/3)

Matti Lindroos[1]
Napat Vajragupta[1]
Janne Heikinheimo[1]
Diogo Ribeiro Costa[2]
Abhishek Biswas[1]
Tom Andersson[1]
Pär Olsson[2]

[1]VTT Technical Research Centre of Finland Ltd
[2]KTH Royal Institute of Technology

Table of contents

1. Introduction

As a part of NKS-R program in 2021, VTT and KTH have studied micromechanical behaviour of UO_2 nuclear fuel pellets to improve understanding of the mechanical deformation processes occurring in the fuel during its usage.

The parabolic temperature profile in the fuel pellet causes tensile stresses at the outer region of the pellet. On the other hand, the inner parts of the pellet experience compressing forces. At the pellet edges, the mechanical behaviour is close to brittle. However, with the elevated temperatures at the central parts of the pellet, the behaviour is more plastic. Stress over the fuel pellet can result diverging local stresses and microcracking due to strain incompatibilities between the grains. Also, porosity, location of pores in grains or at grain boundaries, their size and shape have a strong effect on the UO_2 mechanical behaviour.

The present work proposes a dislocation-density-based crystal plasticity model for UO_2, and polycrystalline microstructures are investigated to analyse plasticity at the grain structure level. Scanning electron microscopy was applied to characterize the sample microstructure. In addition, single and polycrystalline simulations are performed to fit the model parameters with available experimental data. The model has been evaluated and adjusted with different temperatures and strain rates. Furthermore, three different techniques are analysed to introduce porosity within the microstructure. The results have been published in Journal of Nuclear Materials [1]. The NKS report presents the abstract of the work done under NKS-R 2021 project.

2. Material and methods

The UO_2 fuel pellet was supplied by Westinghouse Electric Sweden AB. The pellet was sintered in a hydrogen atmosphere at 1780 °C for about 4 h, which provided a sintered density of 10.5 g/cm^3 (or 96.0 % of UO_2 theoretical density (TD)).

The as-received UO_2 pellet was cut longitudinally and hot-mounted in a phenolic resin with carbon filler for scanning electron microscopy (SEM) and electron backscatter diffraction (EBSD) examinations. The mounted sample was ground with SiC papers (grits 280, 360, and 600) and polished using consecutive diamond suspensions (9, 3, 1, and 0.25 μm). A final polishing treatment with aluminium oxide suspension (0.05 μm, Buhler Masterprep) was performed to provide a defect-free surface for the EBSD analyses. After polished, the sample was coated with a conducting carbon layer (2 nm) for the SEM-EBSD measurements using a Gatan PECS coater.

The crystal plasticity model applies finite strain formalism with a conventional decomposition of deformation gradient to elastic and inelastic contributions. Inelastic deformation by dislocation slip is computed as the sum of all distinguished slip systems.

3. Results and discussion

A crystal plasticity model was proposed to enable investigation of UO_2 deformation behaviour. Both single crystal and polycrystal compression tests were applied in the parametrization of crystal plasticity model. Special attention was placed on the effect of porosity on stress and strain localization. The porosity and grain structure were based on the 2D SEM-EBSD image of a real UO_2 fuel pellet. Also, comparisons were carried out for 3D

simple-element- based approach and explicit 3D porosity structure. All structures were addressed to similar uniaxial compression tests up to 6.8 % of nominal strain.

• The proposed crystal plasticity model includes dislocation-density-based formulation with three slip families. The number of model parameters remains at a reasonable level and temperature effects are included by scaling the model parameters without adding excessive number of fitting parameters. This allows more effective use of a parameter optimization routine.

• The optimization workflow for parameterizing the crystal plasticity model was proposed, which is capable of identifying the parameter set of single crystal and polycrystalline UO2. Mechanical response predicted by single crystal and polycrystalline simulations at 1600K with the strain rate of 0.0001 s^{-1} are in good agreement with experiments performed using similar conditions. Polycrystalline simulations demonstrate strain rate and temperature effects on mechanical behaviour as well. However, compared to the experimental reference, the mismatch is still pronounced, which will be addressed in the follow-up study.

• The results from both 2D and 3D numerical model indicate that the presence of porosity leads to stress localization, which is directly related with the pore volume fraction. With a damage framework in the numerical model, these sites of stress localization can be directly correlated to the onset of damage. The numerical model can be further improved by including a damage model with element deletion method, which could be useful in predicting anisotropic damage behaviour.

• To address the effect of porosity to susceptibility of fuel pellet cracking, the present plasticity model could be extended to include a regularization of slip localization and damage within the framework but with an additional strain gradient term. Furthermore, a model extension to a non-local description of plasticity could be seen beneficial in order to capture the size effects of pores. Finally, it is also apparent that the proposed model could benefit of better estimation of very high temperatures, such as 1900-2000 K, which could require the reformulation of temperature dependent parameters.

4. Conclusions

A dislocation-density-based crystal plasticity model was developed and optimized during the collaborative project of VTT and KTH in 2021. The model enables further development of additional deformation mechanisms, such as cracking at stress localization sites. The work continues under collaborative EU project OperaHPC (OPEn HPC theRmomechanical tools for the development of eAtf fuels).

5. References

[1] M. Lindroos, N. Vajragupta, J. Heikinheimo, D. R. Costa, A. Biswas, T. Andersson, P. Olsson. Micromechanical modeling of single crystal and polycrystalline UO_2 at elevated temperatures. Journal of Nuclear Materials 573, 154127, 2023. https://doi.org/10.1016/j.jnucmat.2022.154127

Bibliographic Data Sheet **NKS-464**

Title	Micromechanical modeling of single crystal and polycrystalline UO_2 at elevated temperatures
Author(s)	Matti Lindroos, Napat Vajragupta, Janne Heikinheimo, Diogo Ribeiro Costa, Abhishek Biswas, Tom Andersson, Pär Olsson
Affiliation(s)	VTT Technical Research Centre of Finland Ltd, KTH Royal Institute of Technology
ISBN	978-87-7893-557-1
Date	November 2022
Project	NKS-R / POMMI (Contract: AFT/NKS-R(21)131/3)
No. of pages	4
No. of tables	0
No. of illustrations	0
No. of references	1

Abstract
max. 2000 characters

Understanding cracking phenomena in polycrystalline UO_2 fuel pellet requires detailed knowledge of the fuel's local microscopic stresses and operational conditions. High stress states emerge in the pellet due to a deep parabolic temperature gradient between the center and cylindrical edges of the pellet. In normal operating conditions, the outer regions of the fuel pellet are brittle and experience tensile stresses. On the other hand, the inner parts of the pellet experience compressive stresses, and the behavior is increasingly plastic. Macroscopic stress in the pellet can cause diverging local stresses and microcracking due to e.g. strain incompatibilities between the grains and dislocation pile-ups. Also, porosity, localization of pores in grains and at grain boundaries, their size, and shape substantially impact UO_2 cracking behavior.

This study proposes a micromechanical modeling workflow to study how pores affect the plasticity of polycrystalline UO_2. SEM-EBSD was performed on standard UO_2 pellets with dense microstructure and round pores at inter and intra-granular locations. The characterized microstructure was meshed and coupled with a dislocation-based crystal plasticity model to simulate the uniaxial compression behavior at 1600 K. To this end, we propose the constitutive model that potentially can describe the deformation of a single crystal and polycrystalline UO_2. We have also developed the inverse optimization method to identify material parameters providing a unique solution at different length scales. With the

element removal technique, we have assessed the influence of pores size, volume fraction, and their distribution in microstructures on the mechanical response of polycrystalline UO_2.

Key words Crystal plasticity, Uranium dioxide, Mechanical behavior, Porosity, Strain localization, SEM-EBSD

Journal of Nuclear Materials 573 (2023) 154127

Contents lists available at ScienceDirect

Journal of Nuclear Materials

journal homepage: www.elsevier.com/locate/jnucmat

Micromechanical modeling of single crystal and polycrystalline UO_2 at elevated temperatures

Matti Lindroos[a,*], Napat Vajragupta[a], Janne Heikinheimo[a], Diogo Ribeiro Costa[b,c], Abhishek Biswas[a], Tom Andersson[a], Pär Olsson[b]

[a] VTT Research Centre of Finland Ltd, Tekniikantie 21, Espoo, Finland
[b] KTH Royal Institute of Technology, Brinellvägen 8, Stockholm, Sweden
[c] Westinghouse Electric Sweden AB, SE-721 63,Västerås, Sweden

ARTICLE INFO

Article history:
Received 10 June 2022
Revised 2 November 2022
Accepted 3 November 2022
Available online 13 November 2022

Keywords:
Crystal plasticity
Uranium dioxide
Mechanical behavior
Porosity
Strain localization
SEM-EBSD

ABSTRACT

Modelling of UO_2 mechanical behavior requires detailed knowledge of the local stresses and strains during the fuel's operation in normal and accident conditions. Therefore, a crystal plasticity formulation is proposed for polycrystalline UO_2. The model contains a dislocation-density-based formulation including three slip families and their interactions. The model is parametrized with single crystal and polycrystal experimental data using an optimization scheme. The model's capability to represent yield point, strain hardening behavior, temperature and strain rate dependencies are evaluated. Finally, different approaches to include porosity at the polycrystal are analyzed to assess the effect of porosity on homogenized macroscopic stress-strain behavior, and stress/strain localization at the grain level.

1. Introduction

Nuclear fuel is one of the central components in a nuclear power plant (NPP). It is the place where fission energy is created. In light water reactors (LWR), the fuel consists of ceramic uranium oxide pellets that are sealed into metallic cladding tubes. Fuel pellets and their cladding form the main barrier against radioactive release containing as intact all fission products created in the fission reactions. From the safety point of view it is therefore important to understand the fuel pellet and fuel rod behaviour in operation and accident conditions. Fuel pellet deformation includes complex physical and chemical phenomena spanning to multiple length and time scales. OECD/NEA State-of-the-art report identifies four key phenomena with the ongoing research programs: creep, swelling, cracking and mechanical deformation in pellet-clad interaction [1].

The parabolic temperature profile in the fuel pellet causes tensile stresses at the outer region of the pellet. On the other hand, the inner parts of the pellet experience compressing forces. At the pellet edges, the mechanical behaviour is close to brittle. However, with the elevated temperatures at the central parts of the pellet, the behaviour is more plastic [2]. Stress over the fuel pellet can result diverging local stresses and microcracking due to strain incompatibilities between the grains [3]. Also porosity, location of pores in grains or at grain boundaries, their size and shape have a strong effect on the UO_2 mechanical behaviour [4–7]. Among other approaches, phase field has been utilized in predicting intergranular brittle fracture strength with different amounts of porosity at the grain boundaries [8]. The study by Chakraborty et al. [8] was limited to a single type of grain boundary and the grain structure was arbitrary. With elevated temperature, plastic deformation mechanisms have increasingly important role in the pellet mechanical behaviour in general. Compression tests of individual polycrystalline fuel pellets have shown that increasing the strain rate at elevated temperature generates strain hardening [3,9]. Strain hardening modelling capability is especially relevant for estimations of the pellet mechanical behaviour in accident scenarios.

Portelette et al. [10] formulated a crystal plasticity model for UO_2 and investigated single crystal plasticity and temperature dependency of the material. In their recent study [11], dislocation dynamics was used to determine slip-slip interaction coefficients to propose a slip interaction hardening matrix addressing three different slip families and their connections. In a recent study [12], they investigated effects of large pores and stress triaxiality with synthetic microstructures with utilizing reduced version of a crystal plasticity model presented in [10]. The effects of small pores within fresh microstructures and their interactions with im-

* Corresponding author.
E-mail address: Matti.Lindroos@vtt.fi (M. Lindroos).

https://doi.org/10.1016/j.jnucmat.2022.154127

age based (EBSD) grain structures was not in the scope of their work.

As irradiation of a fuel element proceeds, both the chemical composition and physical structure of UO_2 pellets evolve. Therefore, it is important to understand separately the impact of defect changes on mechanical properties in real microscopy-based UO_2 pellet structure to further develop models for irradiation effects in UO_2 pellets. It can be argued that investigations focusing on explicit microstructures and existing defect structures are not yet comprehensively presented in literature. The present work proposes a dislocation-density-based crystal plasticity model with various parameters contributing to slip resistance and strain hardening for UO_2. Computational polycrystalline microstructures are investigated to analyze plasticity at the grain structure level with various techniques. The paper is organized as follows. In Section 2, material characterization with scanning electron microscopy and the crystal plasticity model are introduced. In Section 3, single and polycrystal simulations are performed to fit the model parameters with available experimental data utilizing an optimization routine. The model's feasibility is evaluated with respect to different temperatures and strain rates. In the final part of Section 3, we investigate the effect of small or medium sized (smaller than grain size) pores, within polycrystalline UO_2 microstructures, on the material's plastic deformation response. In particular, three different techniques to represent simplified or explicit porosity within the microstructure are analyzed. At the grain scale, the effect of porosity on stress/strain localization is studied, which ultimately has an important role in determining cracking behavior of UO_2 fuel pellets. Section 4 summarizes the obtained results and shortly discusses the future research needs.

2. Material and methods

2.1. Sample and scanning electron microscopy

The UO_2 fuel pellet was supplied by Westinghouse Electric Sweden AB. The pellet was sintered in a hydrogen atmosphere at 1780 °C for about 4 h, which provided a sintered density of 10.5 g/cm^3 (or 96.0% of UO_2 theoretical density (TD) [13]).

The as-received UO_2 pellet was cut longitudinally and hot-mounted in a phenolic resin with carbon filler for scanning electron microscopy (SEM) and electron backscatter diffraction (EBSD) examinations. The mounted sample was ground with SiC papers (grits 280, 360, and 600) and polished using consecutive diamond suspensions (9, 3, 1, and 0.25 μm). A final polishing treatment with aluminium oxide suspension (0.05 μm, Buhler Masterprep) was performed to provide a defect-free surface for the EBSD analyses. After polished, the sample was coated with a conducting carbon layer (2 nm) for the SEM-EBSD measurements using a Gatan PECS coater.

The EBSD analyses were carried out in a high-resolution field emission gun (FEG) SEM model Zeiss GeminiSEM 450, coupled with an EBSD detector (Oxford instruments Synergy) and the software AZTEC. Secondary electron (SE) detector was used to evaluate the microstructure morphology at 1000X magnification (step size: 0.15 μm; matrix: 1333 x 1333 steps). The EBSD results assessed the UO_2 crystal structure, grain orientations (inverse pole figure (IPF) colouring), and Euler angles (EAs). The average grain size (AGS) was computed based on 180 grains, with five measurements per grain, using the software ImageJ [14]. The uncertainty of AGS is reported as one standard deviation.

2.2. Crystal plasticity model

Finite strain formalism is used with a conventional decomposition of deformation gradient $\underline{F}$ to elastic $\underline{F}^E$ and inelastic $\underline{F}^P$ contributions. The decomposition reads:

$$\underline{F} = \underline{F}^E \cdot \underline{F}^P \tag{1}$$

2.3. Dislocation deviated plasticity

Inelastic deformation by dislocation slip is computed as the sum of all distinguished slip systems. The model includes a possibility to deform by three slip families, as was also suggested by Portelette et al. [10], involving six {100} < 110 >, six {110} < 110 > and twelve {111} < 110 > slip systems. The plastic velocity gradient $\underline{L}^p$ then reads:

$$\underline{L}^P = \dot{\underline{F}}^P \cdot \underline{F}^{P-1} = \sum_{s=1}^{6} \dot{\gamma}^s \underline{N}^s + \sum_{s=7}^{12} \dot{\gamma}^s \underline{N}^s + \sum_{s=13}^{24} \dot{\gamma}^s \underline{N}^s \tag{2}$$

where $\dot{\gamma}^s$ is the slip rate and $\underline{N}^s$ is the orientation tensor of a slip system s, respectively. Slip rate of a slip system can be written in the form of rate dependent dislocation motion [15].

$$\dot{\gamma}^s = \left\langle \frac{|\tau^s| - \tau_c^s}{K^{fam}} \right\rangle^n sign(\tau^s) \tag{3}$$

where τ^s is the resolved shear stress of a slip system s and τ_c^s is the effective shear resistance. Parameters K^{fam} and n describe viscous behavior, where superscript fam indicates to different slip families. Exponent n is defined as a function temperature to account for cross-slip at high temperatures. Kinematic hardening is omitted in the present approach for simplicity and in the absence of cyclic stress-strain data.

The shear stress of a slip system, defined as $\tau^s = \underline{M} : \underline{N}^s = (\underline{C}^e \cdot \underline{S}^e) : \underline{N}^s = (\underline{C}^e \cdot (\underline{\underline{\Lambda}} : \underline{E}_{gl})) : \underline{N}^s$, drives the plastic deformation when it exceeds the critical/effective shear resistance τ_c^s. Mandel stress $\underline{M}$ is defined in the intermediate configuration with Green-Lagrange strain tensor $\underline{E}_{gl}$, while $\underline{S}^e$ is the second Piola-Kirchhoff stress tensor, and $\underline{\underline{\Lambda}}$ is the fourth order elastic stiffness tensor. $\underline{C}^e$ is the Cauchy-Green tensor. Denotation $\underline{X}$ refers to a second order tensor, while x denotes a scalar.

The shear resistance of a slip system s includes contributions from lattice friction term τ_0^s, grain size effect realised with a Hall-Petch relation τ_{HP}, and a term for describing dislocation interactions.

$$\tau_c^s = \tau_0^s + \tau_{HP} + \mu b^s \sqrt{\sum_{s=1}^{N^s=24} a_{eff}^{sj} \rho^j} \tag{4}$$

where μ is shear modulus, b^s length of the Burgers vector. Dislocation interaction matrix a^{sj} is adopted from the derivation of the its form in [11], in which superscripts s and j describe interaction between slip systems s and j. It is worth noting that, this leads to a large number of interaction coefficients that hold uncertainty in their effect. Following the work of [16], we utilize evolving interaction coefficients for the effective interaction matrix as:

$$a_{eff}^{sj} = \left(0.2 + 0.8 \frac{ln(0.35 b^s \sqrt{\rho_s})}{ln(0.35 b^s \sqrt{\rho_{ref}})}\right)^2 a^{sj} \tag{5}$$

where ρ_{ref} is a reference dislocation density.

The Hall-Petch relation is conventionally introduced within the crystal plasticity framework by proportionality with inverse square root of the grain size. The Hall-Petch coefficient K_{HP} describes the magnitude of the grain size related hardening. The strengthening effect is scaled with temperature dependent shear modulus in the absence of quantitative experimental data.

$$\tau_{HP} = \frac{\mu(T)}{\mu(300K)} \frac{K_{HP}}{\sqrt{d}} \tag{6}$$

where K_{HP} is Hall-Petch type hardening coefficient, and d is the effective grain size. Similarly we scale friction stress τ_0^s and viscous

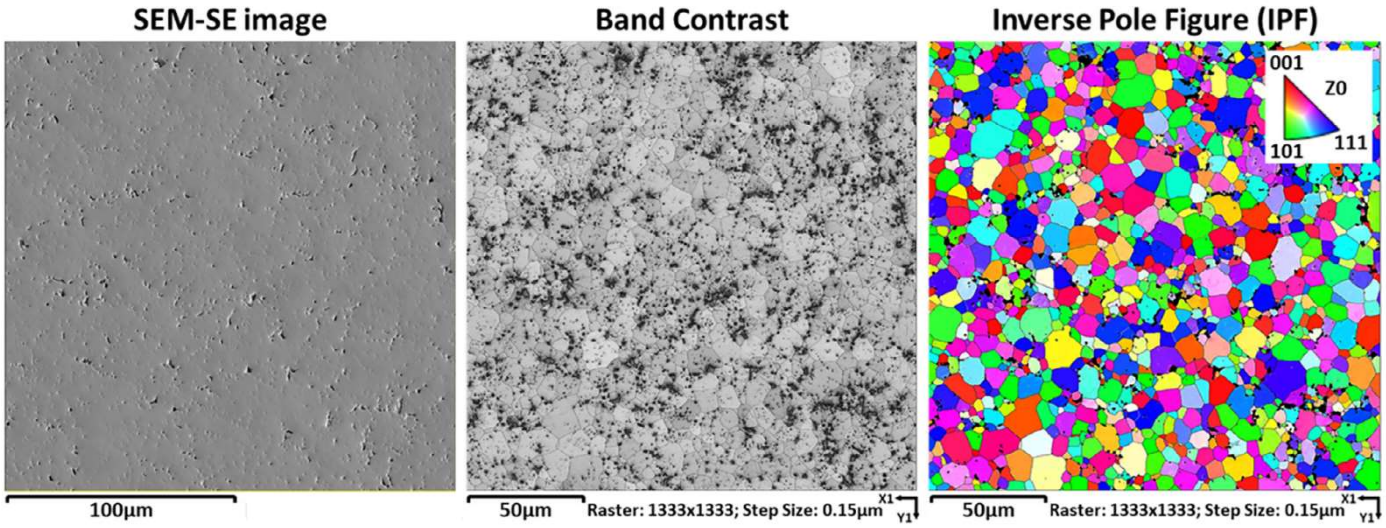

Fig. 1. SEM-EBSD examination of a standard UO_2 fuel pellet. No preferential crystallographic orientation is observed in the IPF image, which is characteristic of the standard polycrystalline UO_2 fuel [19]. The average grain size obtained from the IPF image was 10.6 ± 4.0 µm.

parameter K^{fam} in Eq. (3), to approximate temperature effect on these parameters consistently.

$$\tau_0^s = \frac{\mu(T)}{\mu(300K)}\tau_{0-RT} \tag{7}$$

$$K^{fam} = \frac{\mu(T)}{\mu(300K)}K_0^{fam} \tag{8}$$

The rate of dislocation density is given as a function of mean free path to describe dislocation multiplication and annihilation.

$$\dot{\rho}^s = \frac{|\dot{\gamma}^s|}{b^s}\left(\frac{1}{K_{mfp}}\left[\frac{1}{d} + \frac{\sqrt{\sum_{s=1}^{N_s} a_{sys}^{sj}\rho^s}}{K_{for}^{fam}}\right] - G_c\rho^s\right) \tag{9}$$

where K_{for}^{fam} describes the average number of obstacles overcome before dislocation is immobilized and each slip family have their own obstacle parameter. K_{mfp} is used as fitting parameter to define effective mean free path. Parameter G_c is an approximation of annihilation distance. The effective annihilation distance is chosen as a function of temperature and strain rate to effectively reduce the strain hardening rate at elevated temperatures [17].

$$G_c = G_{c0}\left(\frac{\dot{\gamma}_{ref}}{|\dot{\gamma}^s|}\right)^{(k_BT)/A_{gc}} \tag{10}$$

where k_B is the Boltzmann constant, A_{gc} is a magnitude controlling parameter; and $\dot{\gamma}_{ref}$ is a reference shear rate.

3. Results and discussion

3.1. Material characterization

The SEM-EBSD result in Fig. 1 shows a dense UO_2 microstructure with round and flake-like pores. Its band contrast image reports poorly indexed regions (darker areas) around the pores and well-indexed grains (brighter areas) within the dense UO_2 matrix, as previously reported [18]. No preferential crystallographic orientation is observed in the IPF image, which is characteristic of the standard polycrystalline UO_2 fuel [19]. The average grain size computed based on this IPF image was 10.6 ± 4.0 µm.

The round pores observed in Fig. 1 were present at both intra- and inter-granular positions in the microstructure, which is characteristic of closed porosity at the end of the UO_2 sintering process [20]. It is reported that the flake-like pores are the results of sintering UO_2 powder particles that remained either in their original shape or were slightly deformed during pressing [21]. These unbroken UO_2 particles can create voids (or gaps) with the surrounded UO_2 particles. Thus, these gaps tend to shrink slowly due to their large sizes, and the residual porosity becomes a flake-like pore around the unbroken particles [22].

3.2. Parametrization strategy

Because the crystal plasticity model introduced in this study must be applicable for predicting the mechanical response of UO_2 at different length scales, we propose a multiscale parameterisation strategy. In this context, we established the two-stage parameterization scheme, which considers the mechanical response of UO_2 single crystals and polycrystals at elevated temperatures.

In the first step, the optimisation scheme was set up to parameterize selected crystal plasticity parameters by mimicking stress-strain curves obtained from single crystal compression experiments by simulations. In this context, the generalised optimisation module of Z-set was applied [23]. The general optimisation scheme can be described as follows with the help of Fig. 2a. At the beginning, a simulation is performed with the initial guess material parameters. Results obtained are compared with experimental reference by calculating the objective function. Based on this, the optimisation algorithm suggests a new and more suitable set of material parameters for the new simulation iteration. The entire procedure continues until the tolerance criterion is reached and the optimised parameters set is then obtained. In terms of experimental references, we considered single crystal experiments at 1600K with three different orientations of compression axis (Φ = 13.0°, 25.5°, and 36.0°) as reported in [24] to ensure the solution uniqueness. Note that Φ is the rotation angle from [001] towards [$\bar{1}$11]. Although results of the compression test along other axes (Φ = 2.0°, 44.0°, and 54.0°) were also provided in [24], we neglected them in the parameterization procedure to avoid the chance of the optimized solution not being converged due to an overly complex objective function. With experimental references being identified, the unit cell model of 8 eight-node brick elements (C3D8) were created and solved using the non-linear finite element solver Zébulon [23]. Figure 2b provides the schematic sketch describing boundary conditions applied to the unit cell model, of which the compressive loading direction was parallel to the z-direction. From Figure 2b, the surface 1 was fixed along the y-direction, the surface

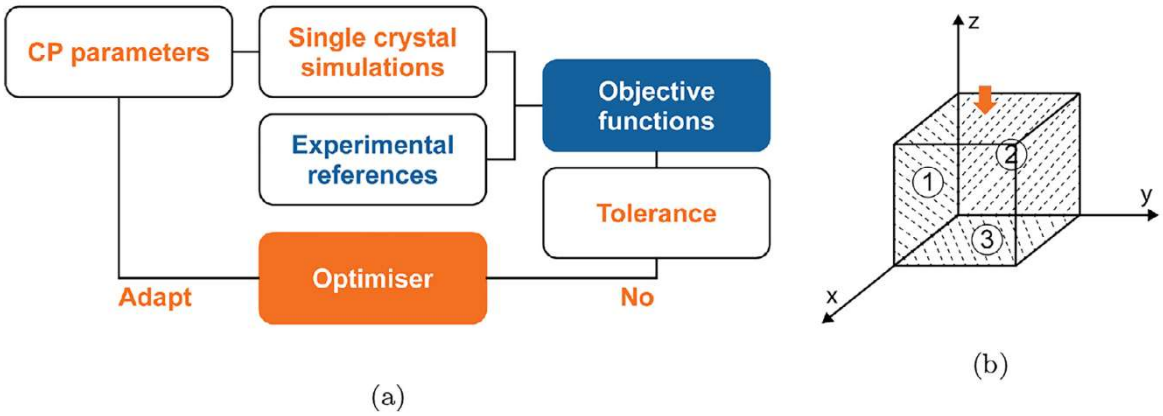

Fig. 2. a) The optimization workflow to parameterize crystal plasticity parameters of UO_2 and b) the schematic sketch describing boundary conditions applied to the single crystal model.

Table 1
Crystal plasticity model parameters.

Elastic constants C_{ij} (1600 K)	$C_{11} = 278$ $C_{12} = 104$ $C_{44} = 54$ [GPa]
Viscous parameter for slip K_0^{100}	9.29 [MPa]
Viscous parameter for slip K_0^{110}	26.03 [MPa]
Viscous parameter for slip K_0^{111}	10.04 [MPa]
Flow exponent $n = ae^{bT} + c$	$a = 182.38\text{x}10^4$, $b = -0.008$, $c = 3.43$
Initial dislocation density $\rho_{ini} = \exp(aT + b)$	$a = -0.0145$, $b = 50.389$ [m^{-2}]
Initial resistance τ_0^{100}	10.73 [MPa]
Initial resistance τ_0^{110}	27.71 [MPa]
Initial resistance τ_0^{111}	33.18 [MPa]
Length of Burgers vector b^s	0.387 [nm]
Obstacle parameter K_{for}^{100}	276.98 [MPa]
Obstacle parameter K_{for}^{110}	227.71 [MPa]
Obstacle parameter K_{for}^{111}	234.17 [MPa]
Mean-free path parameter K_{mfp}	1.62
Annihilation distance G_{c0}	2.9 [nm]
Annihilation parameter A_{gc}	$4.33\text{x}10^{-}20$ [JK^{-1}]
Hall-Petch coefficient K_{HP}	0.5 [MPa$\sqrt{\text{mm}}$]
Effective grain size d_{grain}	10.6 [μm]
Interaction matrix coefficients $a_1 - a_{24}$	adopted from [11]

2 was fixed along the x-direction and the surface 3 was fixed along the z-direction. The strain rate applied was 0.0001 s^{-1} which was similar to the experimental reference [24]. For comparing simulations with experiments, effective stress $\overline{\sigma}$ and effective strain $\overline{\epsilon}$ were homogenised by calculating the spatial average of variables specified over the model volume,

$$\overline{\sigma} = \frac{1}{V}\int_V \sigma \, dV \tag{11}$$

$$\overline{\epsilon} = \frac{1}{V}\int_V \epsilon \, dV \tag{12}$$

Because of their pronounced influence on the stress-strain curve, we focused on identifying τ_0^{100}, τ_0^{110}, τ_0^{111}, K^{100}, K^{110}, K^{111}, n, K_{for}^{100}, K_{for}^{110}, K_{for}^{111}, and K_{mfp} in the first optimisation step. The selected ranges of crystal plasticity parameters were $\tau_0^{100} \in [4, 100]$ MPa, $\tau_0^{110} \in [4, 100]$ MPa, $\tau_0^{111} \in [4, 100]$ MPa, $K^{100} \in [5, 150]$ MPa, $K^{110} \in [4, 250]$ MPa, $K^{111} \in [4, 150]$ MPa, $n \in [8, 17]$, $K_{for}^{100} \in [20, 500]$ MPa, $K_{for}^{110} \in [20, 500]$ MPa, $K_{for}^{111} \in [20, 500]$ MPa, and $K_{mfp} \in [1, 3]$. Other material parameters including elastic constants were taken from literature [25] and summarised in Table 1. To exclude the grain size effect on simulated mechanical response of single crystal, the effective grain size d was defined as 1 mm, which is relatively large.

For the optimisation algorithm, we selected the Nelder-Mead (N-M) method because of its robustness of fitting and it has already been used in [26] to parameterise the non-local crystal plasticity model of tempered martensitic steels from nanoindentation test. The algorithm was firstly proposed by Nelder and Mead [27], of which a space is taken across a subregion and moves from the worst location to the opposite side of the simplex to obtain better solutions. It creates a simplex or a body in n dimensions consisting of $n + 1$ vertices, of which their position describes the simplex completely. The worst vertex iteratively relocates and shrinks to the global minimum in the n-dimensional design room.

With the optimisation algorithm being selected, we derived the objective function to be minimised. To ensure the solution uniqueness obtained from the optimisation process simulations, the objective function f_{tot} considered simulations and experiments with three different orientations of compression axis. Here, all simulations were equally weighted and f_{tot} was defined as

$$f_{tot} := \frac{1}{3}f_{13.0^\circ} + \frac{1}{3}f_{25.5^\circ} + \frac{1}{3}f_{36.0^\circ} \rightarrow min. \tag{13}$$

$f_{13.0^\circ}$, $f_{25.5^\circ}$, and $f_{36.0^\circ}$ are discrepancy functions describing the difference in stress σ for the same applied strain ϵ_k between simulation and experiment of compression test along orientation axis of 13.0°, 25.5°, and 36.0° respectively. In this context, they were determined based on point densities, which is suitable for comparing data with unequal data points. The data with smaller data points will be interpolated between points of the large file. For each compressive loading axis, the discrepancy function f_i is expressed as

$$f_i = \frac{1}{N}\sum_{k=0}^{N}\left[\frac{\sigma_{sim}(\epsilon_k) - \sigma_{exp}(\epsilon_k)}{\sigma_{exp}(\epsilon_k)}\right]^2 \tag{14}$$

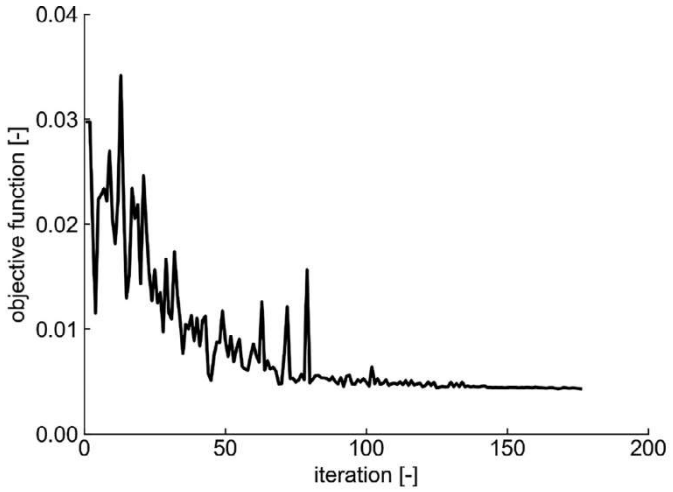

Fig. 3. Evolution of objective function during the optimisation process.

With the derived objective function and the selected optimisation algorithm, we defined the tolerance criteria for finishing the optimisation process. For this study, there are two criteria to be considered. Firstly, the optimisation is stopped once the objective function is lower than 10^{-5}. Secondly, if the first criterion is not fulfilled, the optimisation process comes to an end after the absolute difference in f_{tot} between subsequent iterations $\left|f_{tot}^{i+1} - f_{tot}^{i}\right|$ becomes smaller than 10^{-9}. The solution is then treated as the lowest f_{tot} obtained from all iterations.

Evolution of the objective function during the optimization process is shown Fig. 3. In the beginning, the objective function calculated from the initial parameters set is 0.0297, decreasing exponentially to reach the saturated regime after 100 iterations. The optimization process is terminated after 176 iterations, of which the tolerance criterion is met. The objective function of the optimized parameters set is 0.0043, which is significantly lower than the initial step. We also plotted how material parameters change during the optimization process in Fig. 4. Similar to Fig. 3, all material parameters reach the saturated regime after 100 iterations, and a small adjustment is made to obtain the optimized solution in last iteration. All crystal plasticity parameters identified are summarized in Table 1.

3.3. Mechanical response of densed UO_2

3.3.1. Single crystal

Figure 5 depicts the mechanical response predicted from simulations of the parameterised single crystal. The simulation results of parameterized model are plotted with dash-dotted lines. From the comparison of compressive stress-strain behavior with selected experimental reference plotted in Fig. 5a, a good agreement can be observed, of which crystallographic orientation dependency on the yield stress can be well captured. The parameterised unit cell model can also mimic strain hardening behaviour for $\Phi = 25.0^{\circ}$ and $\Phi = 36.0^{\circ}$. However, it still lacks the ability to capture the steep hardening behaviour for the case of simulation with $\Phi = 13.0^{\circ}$. Because the dislocation deviated plasticity is applied in this study, we can trace how dislocation densities change during the deformation processes as shown in Fig. 5b, of which the evolution of total dislocation density with increasing applied compressive strain was plotted. However, comparing to [28], the total dislocation density predicted was noticeably higher than experimental values reported. In this context, there are several factors affecting the accuracy of a dislocation density estimate, including sample preparation for transmission electron microscopy (TEM). Further investigation on a comparison between dislocation density simulated and estimated by modern microstructure characterisation facility will be the subject of studies planned in the future. We must also note that a good agreement between simulations and experiments might be valid only for the selected compressive load axes because the remaining load axes were not considered in this study, unlike [10] which compared simulations with all load axes.

We also study how interaction matrix and evolving interaction affect stress-strain behavior and dislocation density evolution of single crystal UO_2 as plotted in Fig. 5. Dashed lines refer to simulations excluding the interaction matrix, and dotted lines stand for simulations neglecting the evolving interaction. Without considering the interaction matrix in the crystal plasticity flow rule, ideal plasticity behavior is exhibited, of which no strain hardening behavior is observed once initiating the plastic yielding (excluding self-interaction also). Furthermore, compared to simulations of the parameterized model, the total dislocation density remains low, indicating to very small multiplication. Moreover, for simulations without evolving interaction, we observe a subtle difference in strain hardening behavior and total dislocation density evolution. One of the reasons for these results is that the strain rate applied to these simulations is relatively low ($10^{-4}\ s^{-1}$), which minimizes the effect of this evolving term.

3.3.2. Polycrystal

With the crystal plasticity parameters being identified for a single crystal UO_2, they are applied to the polycrystalline UO_2 model, generated using the Voronoi tessellation. The model consists of 250 grains with random crystallographic orientations to avoid the crystallographic texture effect on the mechanical response. Note that d_{grain} is now assigned as 10 μm, which is identical to the average grain size identified by EBSD analysis in Section 3.1. To this end, we have compared compressive behavior simulated at 1600K with the experimental reference [3], performed at 1623K with the strain rate of 10^{-4}. Note that we assumed that there is no substantial difference between mechanical response UO_2 polycrystal at 1623K and 1600K. Macroscopic stress and strain are homogenized by following Eqs. (11) and (12). Stress-strain behavior predicted by micromechanical simulations is then plotted in Fig. 6. Note that we compared only the plasticity part of UO_2 polycrystal, of which the engineering stress-true strain curves were all converted to true stress-true strain curves, and the elastic ranges and the elastic-plastic transition were neglected. We then applied the 0.2% offset method on the true stress-true strain curve to identify the yield stress and calculate plastic strain. Comparing the experimental result (black line) with simulated stress-strain behavior (blue line) shows differences in plastic yielding and strain hardening behavior. Therefore, to accommodate the mismatch between experiment and simulation, we increase K_{HP} from 0.0 to 0.5 MPa$\sqrt{\text{mm}}$ to promote the grain size effect on the plastic yielding, of which the result is plotted as the red line. With this adjustment, simulated stress-strain behavior is now in good agreement with the experimental reference, and this parameter set is then used in the next sections.

3.3.3. Strain rate dependency

In this section, we study the influence of strain rate on the mechanical response of polycrystalline UO_2 with optimized crystal plasticity parameters, of which results are compared with compression tests [3] performed at 1600K with strain rates of 0.1, 0.01, 0.001, and 0.0001 s^{-1}. In this context, we perform compression simulations on the parameterized model at 1600K with similar strain rates as experiments. These simulations are plotted with dash-dotted lines. From the strain hardening comparison in Fig. 7a, the parameterized polycrystalline model can capture the experiment performed at the strain rate of 0.0001 s^{-1}. However, the ef-

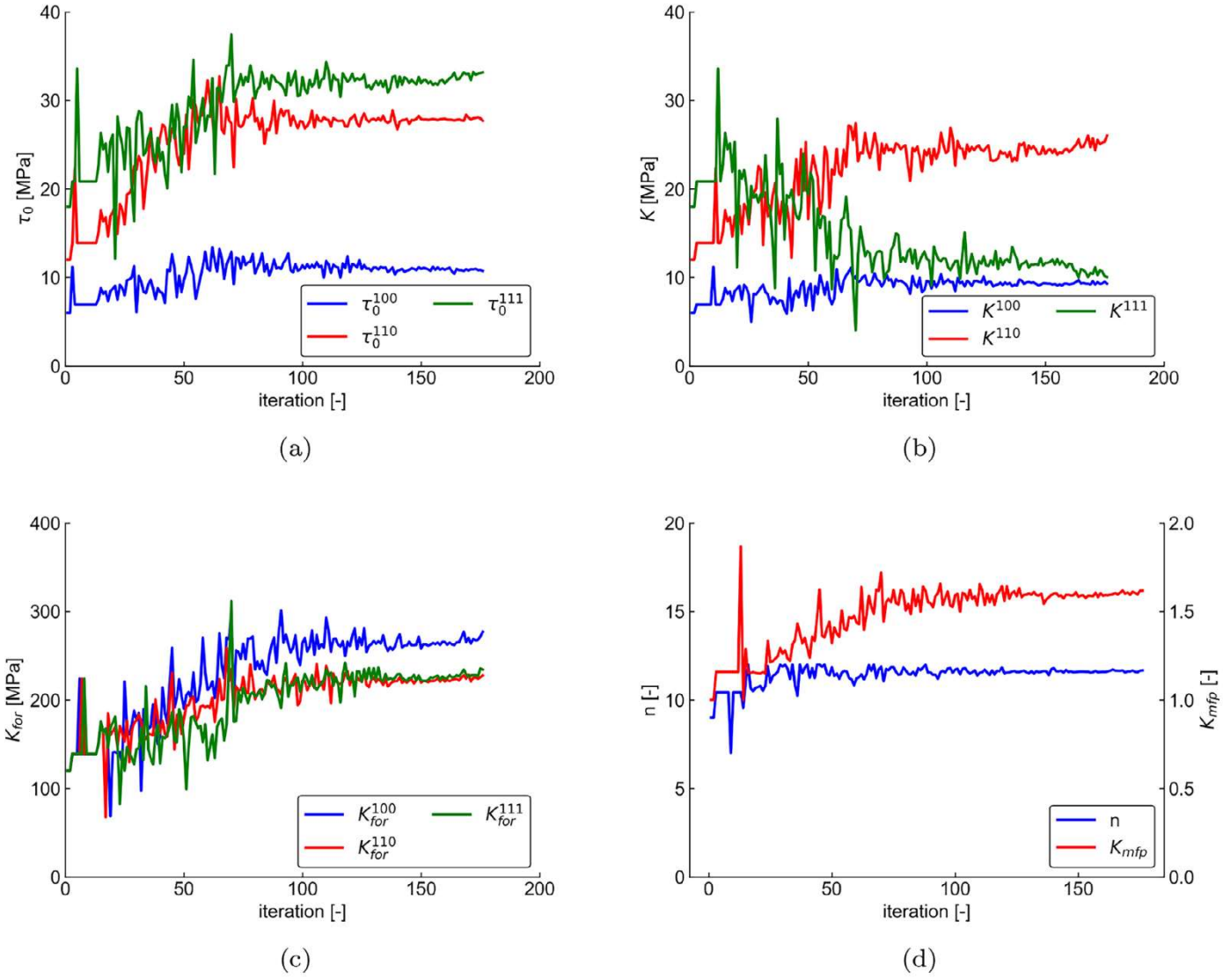

Fig. 4. Evolution of material parameters during the optimisation process: a) τ_0^{100}, τ_0^{110}, and τ_0^{111}, b) K^{100}, K^{110}, and K^{111}, c) K_{for}^{100}, K_{for}^{110}, and K_{for}^{111}, and d) n and K_{mfp}.

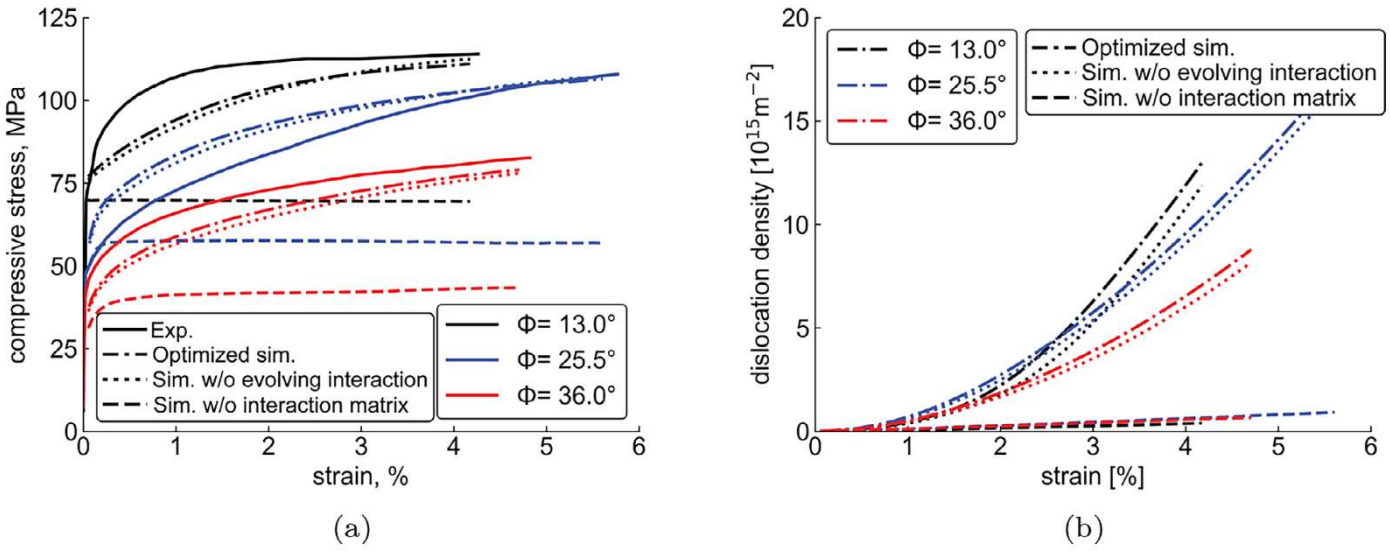

Fig. 5. Simulated mechanical responses of parameterised unit cell models: a) compressive stress-strain behaviour and comparison with experimental reference, and b) evolution of total dislocation density with applied compressive strain. Dash-dotted lines represent simulations with all terms being considered, dotted lines stand for simulations neglecting the evolving interaction, and dashed lines refer to simulations excluding the interaction matrix.

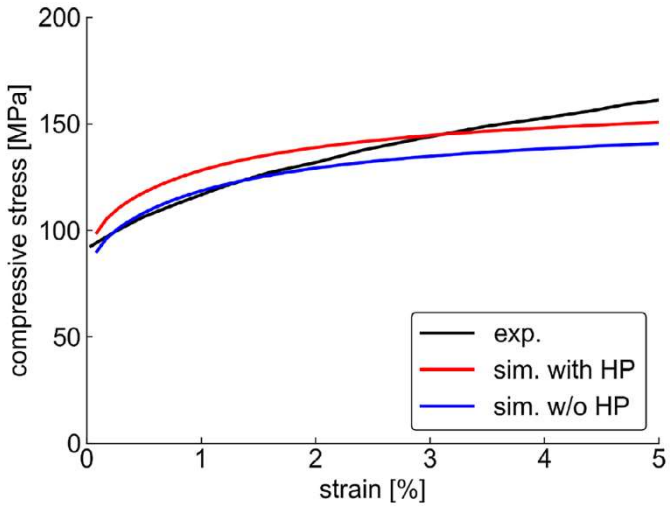

Fig. 6. Stress-strain behaviour comparison between parameterised polycrystal simulation and experimental reference.

fect of strain rate on simulated compressive stress-strain curves is much more pronounced at higher strain rates than in the reference data. Furthermore, we also calculate 0.2, 0.5, and 1.0 % offset yield stresses at different strain rates. From Fig. 7b, the influence of strain rate on an offset yield stress is less prominent than in the experiment, which shows exponential behavior. For improving the crystal plasticity model, it is recommended to include the term, which also considers the strain rate sensitivity to the deformation behavior.

We also perform simulations by neglecting evolving interaction as plotted using dotted lines in Fig. 7a and 7 b. By excluding the evolving interaction term, the effect of strain rate on the strain hardening behavior is even more noticeable than in simulations with the evolving interaction. However, offset yield stresses (Fig. 7b) are more or less similar to simulations with the evolving interaction.

3.3.4. Temperature dependency

Because UO_2 pellets are usually being exposed at an elevated temperature, we study the model capability to predict the temperature influence in this section. The focus is on compression tests performed on polycrystalline UO_2 at 1373, 1600, 1823, and 1973K with the strain rate of 0.0001 s^{-1} [3]. To match experimental reference, we adapt n and initial dislocation density ρ_{ini} as plotted in Fig. 8c and d. Here n and ρ_{ini} are assumed to be temperature dependent and decrease with increasing temperature to accommodate the increased annihilation. Note that comparing to the compression simulation at 1600K, n and ρ_{ini} were larger for the simulation at 1373K. We also fit identified n and ρ_{ini} as a function of temperature T with exponential function, which is provided in Table 1. From the compressive stress-strain comparison in Fig. 8a and b, even though simulations are not in excellent agreement with reference data, they are still able to demonstrate the temperature effects on strain hardening behavior and offset yield stresses. Note that dash-dotted lines represent simulations and solid lines refer to experimental references. At the lower temperature (1373K), the hardening behavior is much more pronounced than simulations at higher temperatures (1823 and 1973K) because the dislocation density annihilation rate is stronger at a higher temperature. The similar reason can be used to explain temperature effect on offset yield stresses as well. By increasing n together with ρ_{ini}, compressive stress-strain behavior and yield stress at 1373K can be captured. However, even though the influence of temperature on the mechanical response is pronounced with decreasing n and ρ_{ini}, discrepancy between experiments and simulations still exists. Further model improvement is required to better capture the temperature effect on the mechanical response of UO_2 in particular at higher temperatures. It is worth noting that yield point of the material is controlled also by Hall-Petch effect τ_{HP} and friction stress τ_0^s besides dislocation density. We suggest a temperature dependent scaling on these effects in Eqs. (6) and (7). It is indicated that the scaling on these parameters is not strong enough to sufficiently decrease the initial yield at high temperatures, given that initial dislocation density cannot be decreased endlessly and in an non-physical manner to achieve a better fit.

3.4. Polycrystal with porosity

Further investigation were performed on porous polycrystal microstructures. Three approaches were used. Figure 9 shows typical examples of the used microstructural aggregates. The first simplistic approach is to assign certain amount of the elements to rep-

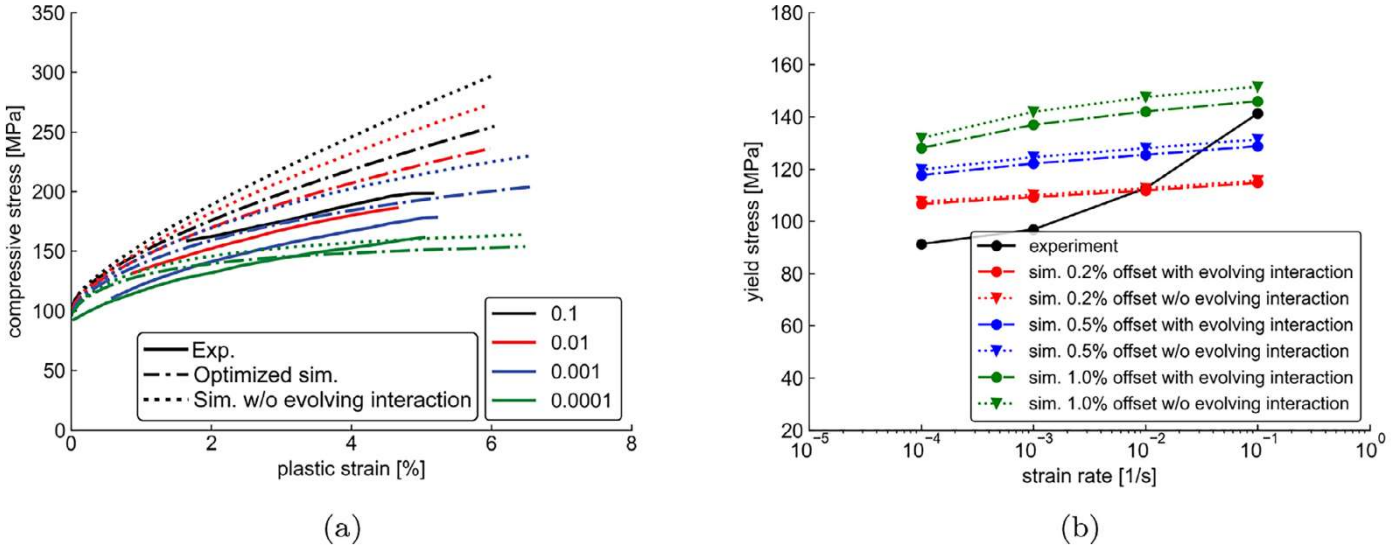

Fig. 7. Simulated mechanical responses of parameterised polycrystalline UO_2 at 1600K with strain rates of 0.1, 0.01, 0.001, and 0.0001 s^{-1}: a) compressive stress-strain behaviour and comparison with experimental reference, and b) Comparison of 0.2, 0.5, and 1.0 % offset yield stresses with experimental reference.

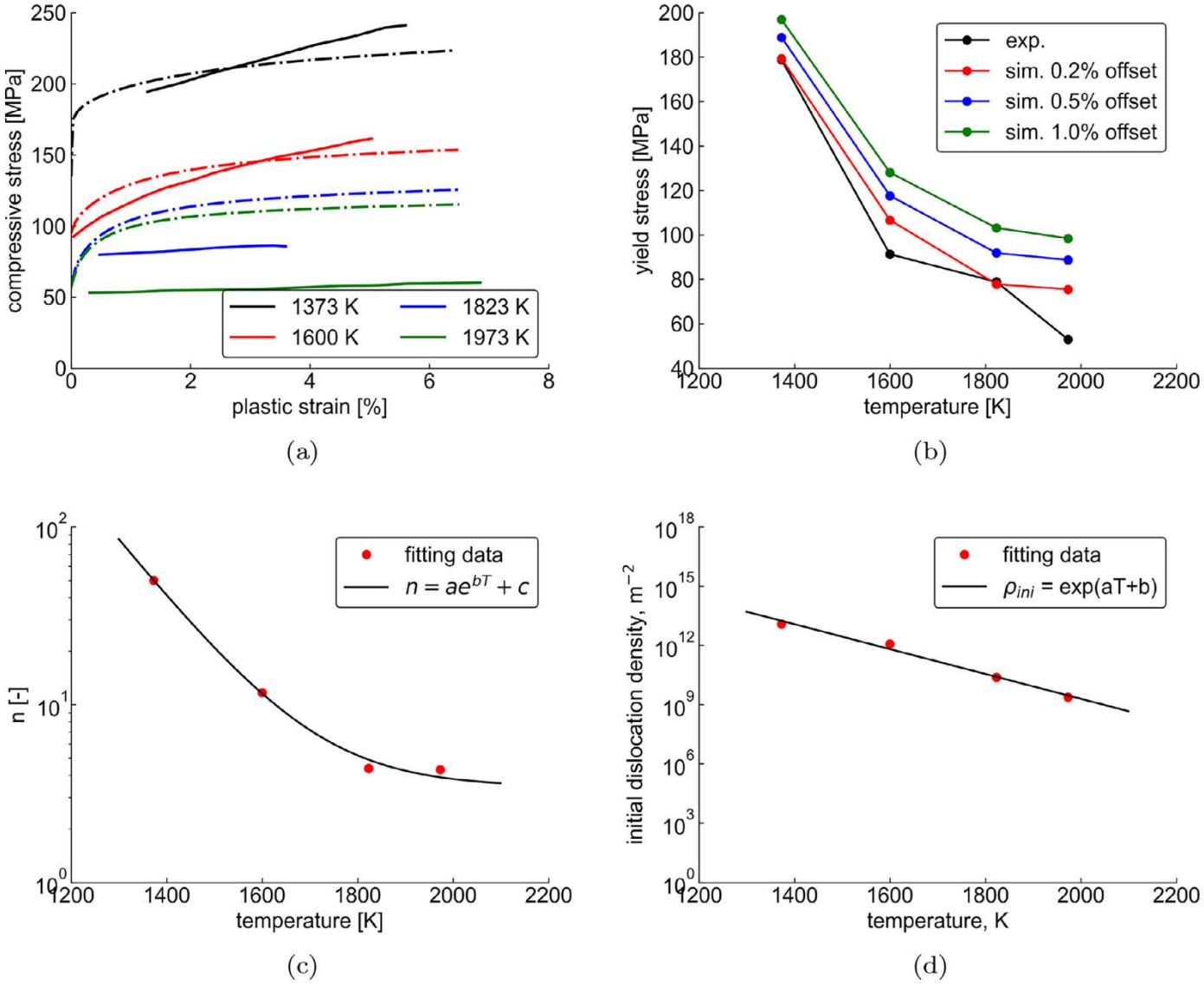

Fig. 8. Simulated mechanical responses of parameterised unit cell models: a) compressive stress-strain behaviour at different temperatures, b) temperature dependency of flow stress, c) fitting of parameter n as a function of temperature, d) fitting of initial dislocation density ρ_{ini} as a function of temperature. Dash-dotted lines represent simulations and solid lines refer to experimental references.

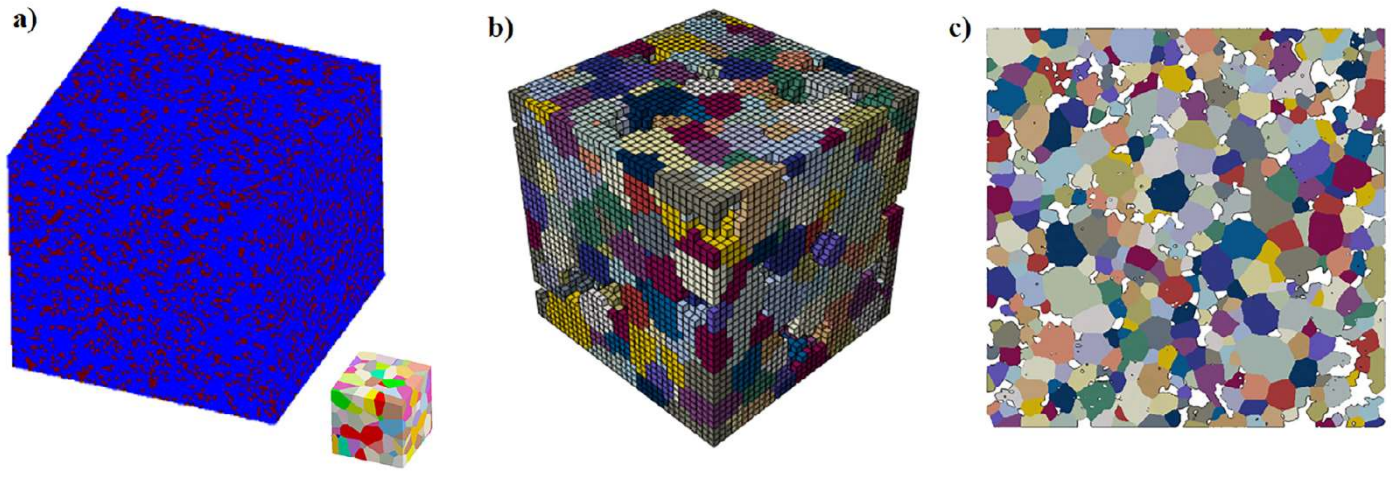

Fig. 9. Polycrystal microstructures with porosity, a) simple-element-based approach, b) explicit 3D porosity, c) EBSD based method. Colours present grain identification number not IPF-colours.

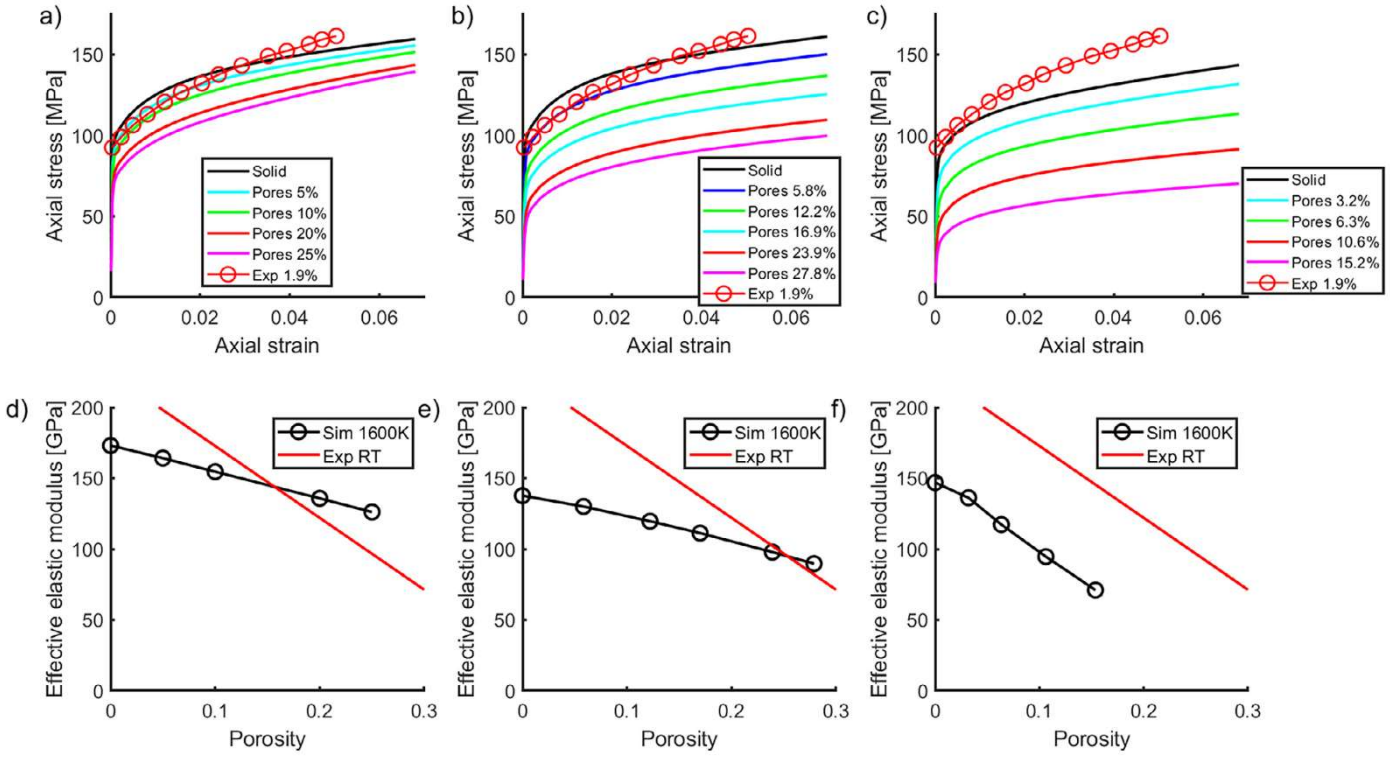

Fig. 10. Stress-strain curves and effective elastic modulus of the microstructures as a function of porosity, a,d) with simple porosity model, b,e) with pore-region model, and c-f) EBSD based simulation model. RT refers to room temperature, while simulations were performed at 1600 K. Experimental curve and the approximated level of porosity extracted from [3].

resent porous phase within solid matrix. In the second approach, larger sections are removed from the material to generate explicit large voids. The third approach includes an identification of porous phase from the EBSD maps. Typical kinematic uniform boundary conditions were chosen for the cases show in Fig. 9a,b. Effectively, despite the porosity at the edges of the aggregates, the exterior faces essentially remain flat in the simulations. The EBSD based microstructure was extruded to one element thickness and the exterior faces are constrained to remain flat also.

Whenever higher porosity is analyzed, the input microstructural aggregates are modified to involve more of porous phase artificially. Then the porosity levels are assigned to range between fully solid (0%) up to very high value of 25% with 5–10% increments depending on the actualization of added porosity. In the case of element-based porosity (Fig. 9a), the regions are assigned as soft elastic with 1 GPa of elastic modulus, whereas the two other cases have simply pores/voids explicitely in the microstructure while maintaining fairly small size of the pores. The crystal plasticity model is then used to evaluate the stress-strain response of the material once porosity increases. The EBSD based computational domains were constructed by obtaining the orientation data from a SEM-EBSD measurement in Fig. 1 following Euler angle convention that are then meshed according to the identified grains.

For the two full 3D polycrystal cases as well as for the EBSD based mesh an axial compression test is performed up to 6.8% strain level at the nominal strain rate of $1 \cdot 10^{-4}$ s^{-1}. It is worth noting that with the EBSD microstructure, the relative number of non-indexed points was 4.2 % of the total number of $7.5 \cdot 10^5$ orientation points in the original measurement data. As the relative number of non-indexed points is close to the nominal porosity, it is reasonable to assume that majority of the non-indexed points represent porous phases of the material. Also, the IPF map in Fig. 1 shows small non-indexed regions in the grains and larger regions at the grain boundaries. This is in line with the SEM examinations by Salvo et al. where finer pores with diameter less than 3 μm are found in the grains and larger ones at the grain boundaries [3].

Figure 10 shows the simulated stress-strain curves for three different approaches following the order of the microstructures shown in Fig. 9.

The apparent stress levels are decreased as a function of the porosity. It is also clear that the simple porosity model, having one element as one pore, shows lower effect on stress-strain behavior than the more detailed porosity model of the EBSD domain or explicit pore 3D model. The best fit with respect to experimental data is observed with the explicit pore model in Fig. 10b. When the effective elastic modulus is defined from the elastic part of the simulated stress-strain curve, a rather linear decrease is observed for all cases, as expected for porous materials. The use of extruded 2D microstructures (EBSD) is not ideal to analyze the complex three dimensional stress state near the pores. However, the EBSD based approach introduces realistic grain structure and qualitative first analyzes maybe performed with the model in terms of stress/strain localization. Furthermore, the discretization related of using single elements as pores poses crude approximation of the stress state near the pores due to lacking mesh details around the pore, which is again non-ideal for any future fracture studies.

Figure 11 shows probability density plots of cumulative plastic slip and Von Mises stress at the end of the simulations with 6.8% of macroscopic compressive strain. The data contains all the integration points within the meshes. Intuitive bimodal distributions are observed for localization of plastic slip and Von Mises stress for element-based porosity in Fig. 11a,b. For the explicit pore model and for the EBSD based model, the distributions illustrate more variation due to the capability to represent stress and strain localization near the pores. Increase in porosity promotes formation of slip rich regimes and also increases the occurrence of higher equivalent stresses.

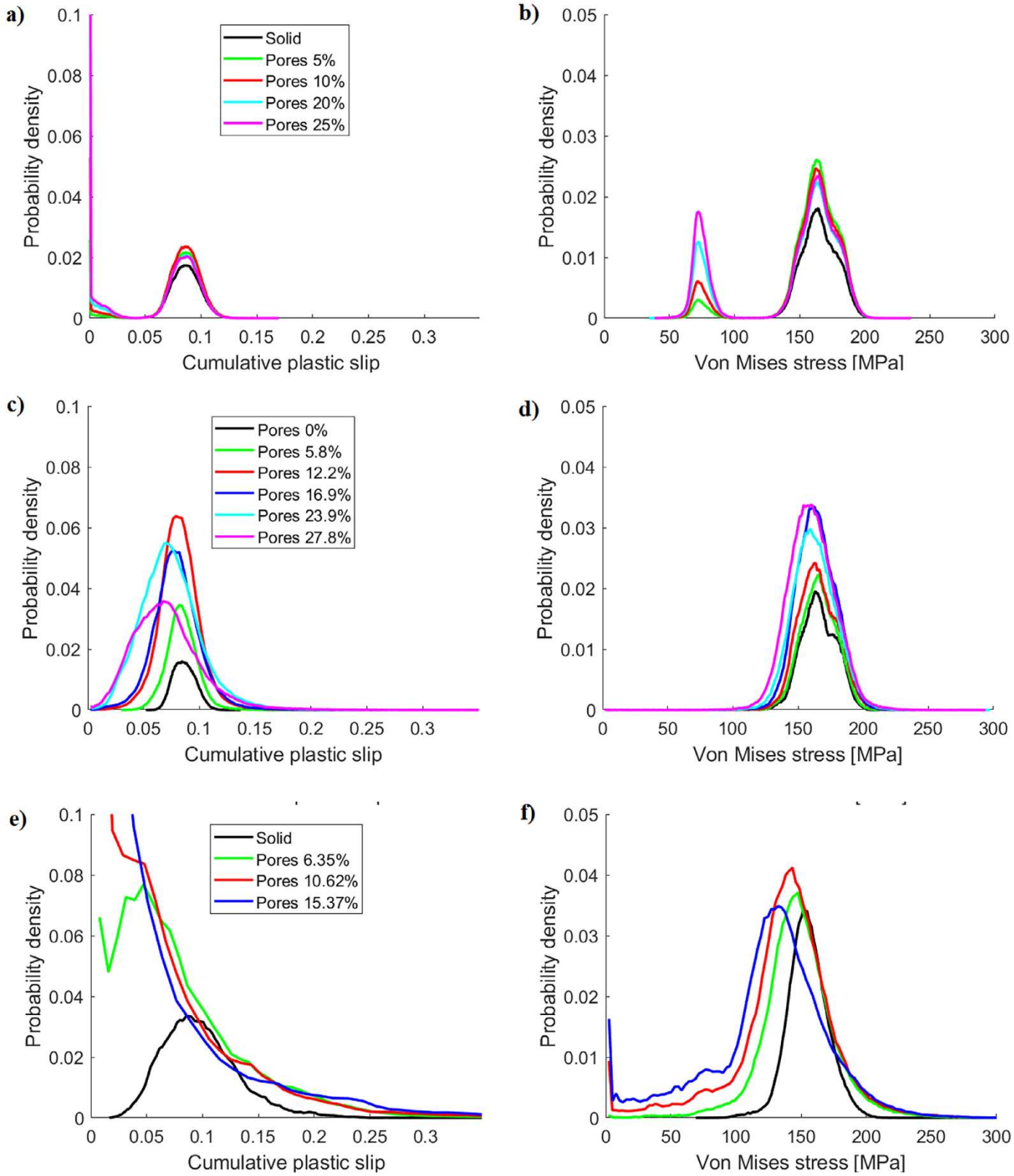

Fig. 11. Distribution of cumulative plastic slip and Von Mises stress for non-porous and porous microstructures, a,b) single element porosity, c,d) explicit pores in 3D polycrystal, and e-f) EBSD based approach.

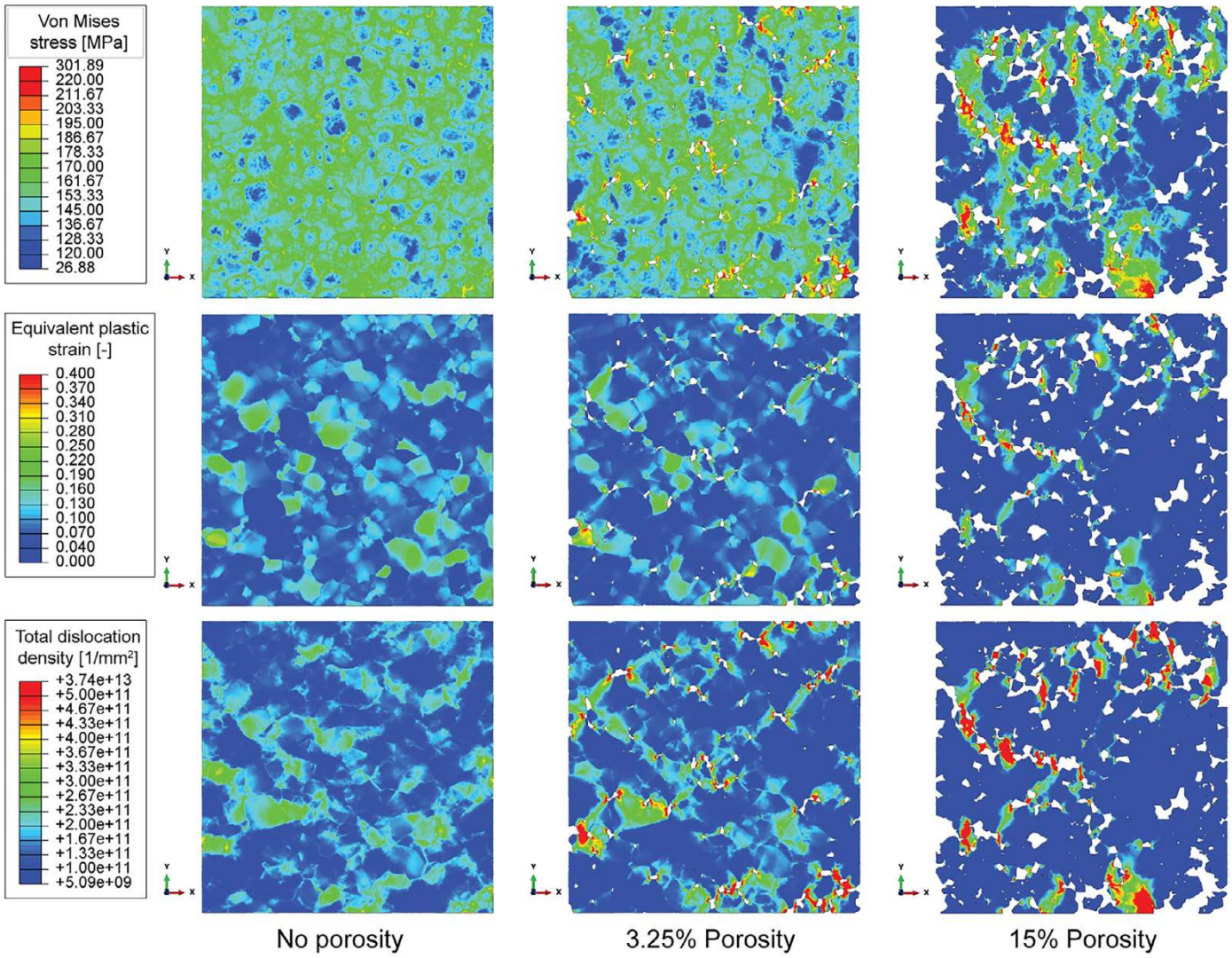

Fig. 12. Comparison von Mises stress, equivalent plastic strain, and total dislocation density contour of simulated EBSD based models with evolving porosity fraction.

In all simulations, the overall dislocation density reaches generally very high values in the range of $1 \cdot 10^{14} - 10^{16}$ m^{-2} after deformation, which are in the range reported in [29,30]. It is noteworthy that high burn-up in the material and related formation of fission products affect the quantity and characteristics of dislocation density, which are not comparable with the fresh fuel pellet. The effect of dislocation loop density is not explicitly included as a defect density in Eq. (4). However, additional dislocation loop defect density can be included, which effectively modifies the slip resistance [16]. In addition, it is worth noting that since damage model is not included in the present analysis, the high porosity levels would be expected to cause fracture of the material before such overall high strain levels, at least locally.

In Fig. 12, we compare von Mises stress, equivalent plastic strain, and total dislocation density distribution of simulated EBSD-based models with evolving porosity fraction. For the model with no porosity, higher von Mises stress concentration can be observed along grain boundaries of UO_2 grains, reflecting dislocation slips being blocked/interfered. When the porosity fraction increases, von Mises stress is localized in the region where porosities are near each other. One can observe the porosity network with localized von Mises stress in the model with a large porosity fraction (15%). Similarly, equivalent plastic strain concentrates in the region between porosity and forms the network of the area with high equivalent plastic strain as well. From the crystal plasticity model introduced in Section 2.2, dislocation densities are the plastic deformation's source, resulting in the total dislocation density distribution in the microstructure conforming to the equivalent plastic strain contour as expected.

Figure 13 illustrates the evolution of von Mises stress, equivalent plastic strain, and total dislocation density contour during the compression simulations of polycrystalline UO_2 with 10% and 25% porosity volume fraction. Both simulations provide a similar trend, starting with large values of von Mises stress, equivalent plastic strain, and total dislocation density provoked in the porosity's vicinity. These concentrated regions then grow and link with others to form a network of localized stress and strain concentration, which can potentially promote damage onset and propagation. The key difference between a model with smaller and larger porosity volume fractions is that the formation of these networks is more pronounced. Simulation results shed light on how porosity, which increases during the operation, affects the mechanical response of polycrystalline UO_2 pellets. To this end, UO_2 pellets with more porosity tend to be more prone to stress and strain localization which can result in damage onset and propagation.

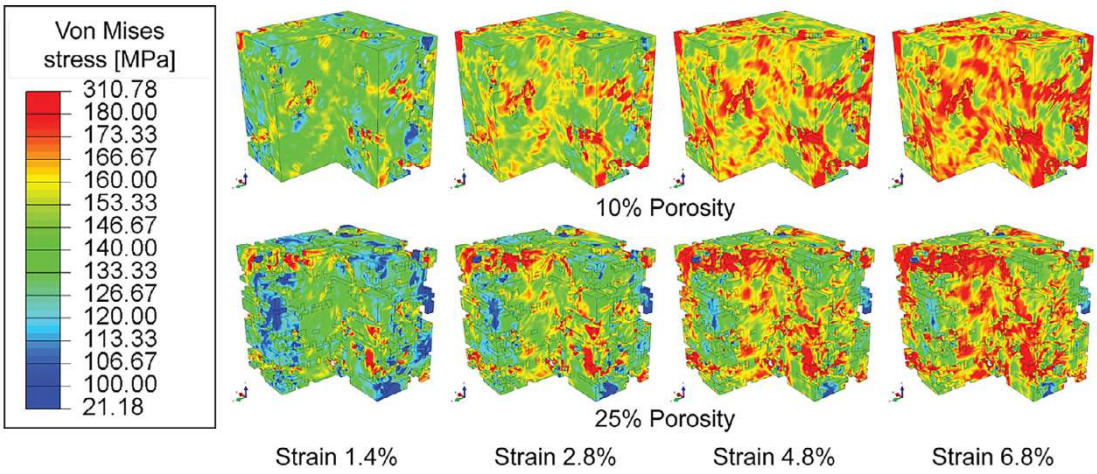

(a)

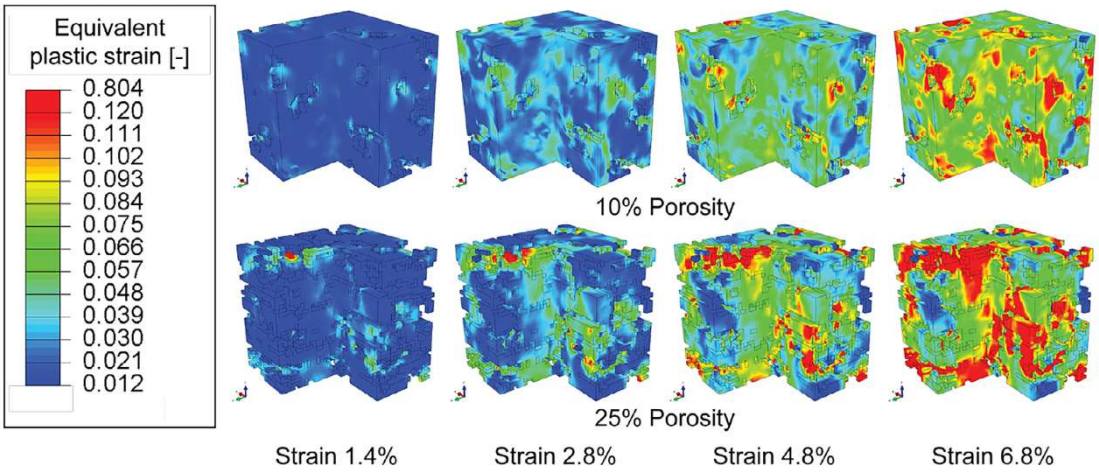

(b)

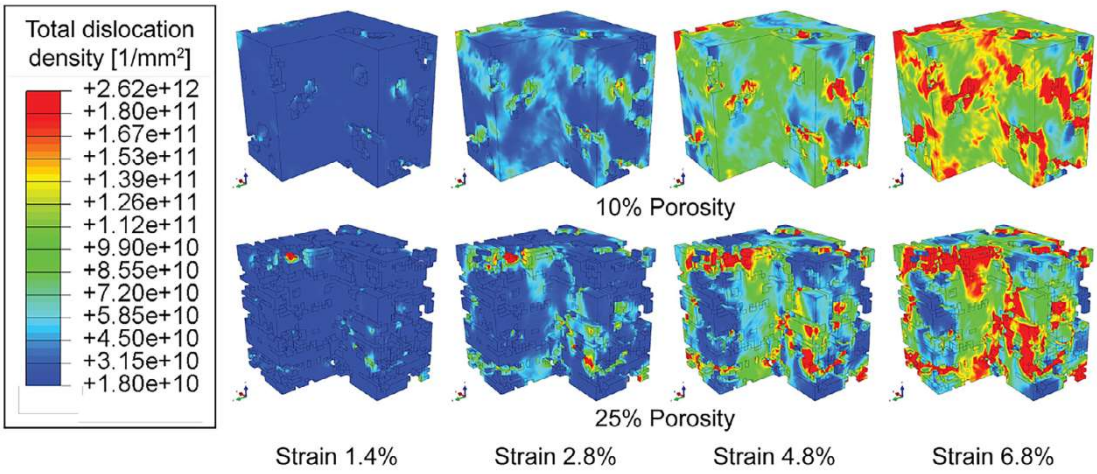

(c)

Fig. 13. Comparison of a) von Mises stress, b) equivalent plastic strain, and c) total dislocation density contour of porous 3D cases.

4. Conclusions

A crystal plasticity model was proposed to enable investigation of UO_2 deformation behavior. Both single crystal and polycrystal compression tests were applied in the parametrization of crystal plasticity model. Special attention was placed on the effect of porosity on stress and strain localization. The porosity and grain structure were based on the 2D SEM-EBSD image of a real UO_2 fuel pellet. Also, comparisons were carried out for 3D simple-element-based approach and explicit 3D porosity structure. All structures were addressed to similar uniaxial compression tests up to 6.8% of nominal strain.

- The proposed crystal plasticity model includes dislocation-density-based formulation with three slip families. The amount of model parameters remains at a reasonable level and temperature effects are included by scaling the model parameters without adding excessive amount of fitting parameters. This allows more effective use of a parameter optimization routine.
- The optimization workflow for parameterizing the crystal plasticity model was proposed, which is capable of identifying the parameter set of single crystal and polycrystalline UO_2. Mechanical response predicted by single crystal and polycrystalline simulations at 1600K with the strain rate of 0.0001 s^{-1} are in good agreement with experiments performed using similar conditions. Polycrystalline simulations demonstrate strain rate and temperature effects on mechanical behavior as well. However, compared to the experimental reference, the mismatch is still pronounced, which will be addressed in the follow-up study.
- The results from both 2D and 3D numerical model indicate that the presence of porosity leads to stress localization, which is directly related with the pore volume fraction. With a damage framework in the numerical model, these sites of stress localization can be directly co-related to the onset of damage. The numerical model can be further improved by including a damage model with element deletion method, which could be useful in predicting anisotropic damage behavior [31].
- To address the effect of porosity to susceptibility of fuel pellet cracking, the present plasticity model could be extended to include a regularization of slip localization and damage within the framework but with an additional strain gradient term (e.g., see ref.[32,33]). Furthermore, a model extension to a non-local description of plasticity could be seen beneficial in order to capture the size effects of pores. Finally, it is also apparent that the proposed model could benefit of better estimation of very high temperatures, such as 1900–2000 K, which could require the reformulation of temperature dependent parameters.

Credit Author Statement

Matti Lindroos, Napat Vajragupta, Janne Heikinheimo, Abhishek Biswas, Tom Andersson, Conceptualization, software, investigation, methodology, validation, writing & editing.

Diogo Ribeiro Costa, Experiments, data curation, methodology, investigation, writing & editing.

Pär Olsson, Conceptualization, methodology, writing & editing.,

Declaration of Competing Interest

The authors declare that they have no known competing financial interests or personal relationships that could have appeared to influence the work reported in this paper.

Data Availability

The authors do not have permission to share data.

Acknowledgments

This work was funded by NKS (Nordic Nuclear Safety Research), SAFIR2022 (The Finnish Research Programme on Nuclear Power Plant Safety 2019–2022) and KYT2022 (Finnish Research Programme on Nuclear Waste Management 2019–2022). Also, Diogo Ribeiro Costa was financially supported by the Swedish Foundation for Strategic Research (SSF, Stiftelsen für Strategisk Forskning), under the project reference number ID17-0078.

References

[1] OECD/NEA, State-of-the-Art Report on Multi-Scale Modelling of Nuclear Fuels, NEA/NSC/R/(2015)5.
[2] R.F. Canon, J.T.A. Roberts, R.J. Beals, Deformation of UO2 at high temperatures, J. Am. Ceram. Soc. 54 (2) (1971) 105–112, doi:10.1111/j.1151-2916.1971.tb12230.x.
[3] M. Salvo, J. Sercombe, T. Helfer, P. Sornay, T. Désoyer, Experimental characterization and modeling of UO2 grain boundary cracking at high temperatures and high strain rates, J. Nucl. Mater. 460 (2015) 184–199, doi:10.1016/j.jnucmat.2015.02.018.
[4] N. Igata, K. Domoto, Fracture stress and elastic modulus of uranium dioxide including excess oxygen, J. Nucl. Mater. 45 (4) (1973) 317–322, doi:10.1016/0022-3115(73)90165-7.
[5] K.C. Radford, Effect of fabrication parameters and microstructure on the mechanical strength of UO2 fuel pellets, J. Nucl. Mater. 84 (1) (1979) 222–236, doi:10.1016/0022-3115(79)90165-X.
[6] M. Oguma, Microstructure effects on fracture strength of UO2 fuel pellets, J. Nucl. Sci. Technol. 19 (12) (1982) 1005–1014, doi:10.3327/jnst.19.1005.
[7] P. Werner, J.L. Routbort, Effect of pore shape on the fracture of UO2 up to high strain rates, J. Nucl. Mater. 113 (1) (1983) 118–121, doi:10.1016/0022-3115(83)90172-1.
[8] P. Chakraborty, Y. Zhang, M.R. Tonks, Multi-scale modeling of microstructure dependent intergranular brittle fracture using a quantitative phase-field based method, Comput. Mater. Sci 113 (2016) 38–52, doi:10.1016/J.COMMATSCI.2015.11.010.
[9] T. Tachibana, H. Furuya, M. Koizumi, Dependence on strain rate and temperature shown by yield stress of uranium dioxide, J. Nucl. Sci. Technol. 13 (9) (1976) 497–502, doi:10.3327/jnst.13.497.
[10] L. Portelette, J. Amodeo, R. Madec, J. Soulacroix, T. Helfer, B. Michel, Crystal viscoplastic modeling of UO2 single crystal, J. Nucl. Mater. 510 (2018) 635–643.
[11] L. Portelette, J. Amodeo, R. Madec, B. Michel, Athermal dislocation strengthening in UO2, J. Nucl. Mater. 538 (2020) 152157.
[12] L. Portelette, P. Vincent, H. Moulinec, M. Gârânau, Micromechanical strain gradient approach to plasticity and damage in martensitic steels, Int. J. Solids Struct. 236–237 (2022) 111316.
[13] R. Rundle, A. Wilson, N. Baenziger, R. Mcdonald, The structures of the carbides, nitrides and oxides of uranium, J. Am. Chem. Soc. 70 (1948) 99–105.
[14] M. Abràmoff, P. Magalhães, S. Ram, Image processing with imagej, Biophotonics Int. 11 (2004) 36–42.
[15] G. Cailletaud, A micromechanical approach to inelastic behaviour of metals, Int. J. Plast. 8 (1992) 55–73.
[16] G. Monnet, C. Mai, Multiscale modeling of crystal plasticity in reactor pressure vessel steels: prediction of irradiation hardening, J. Nucl. Mater. 514 (2019) 128–138.
[17] C.A. Bronkhorst, J.R. Mayeur, V. Livescu, R. Pokharel, D.W. Brown, G.T. Gray III, Structural representation of additively manufactured 316l austenitic stainless steel, Int. J. Plast. 118 (2019) 70–86.
[18] M. Tummalapalli, J. Szpunar, A. Prasad, L. Malakkal, L. Bichler, Evaluation of thermophysical properties of UO2-10 vol% mo nuclear fuel pellets, J. Nucl. Mater. 559 (2022) 153444.
[19] O. Maslova, X. Iltis, L. Desgranges, M. Ammar, C. Genevois, E. de Bilbao, A. Canizarès, S. Barannikova, I. Leontyv, P. Simon, Characterization of an UO2 ceramic via raman imaging and electron back-scattering diffraction, Mater. Charact. 147 (2019) 280–285.
[20] R. German, Sintering: from Empirical Observations to Scientific Principles, first ed., Oxford, 2014.
[21] K. Song, D. Sohn, W. Choo, Effects of sintering processes on the duplex grain structure of UO2, J. Nucl. Mater. 200 (1993) 41–49.
[22] K. Song, K. Kim, Y. Kim, K. Kang, Y. Jung, Reduction of the open porosity of UO2 pellets through pore structure control, J. Nucl. Mater. 279 (2000) 253–258.
[23] J. Besson, R. Foerch, Object-oriented programming applied to the finite element method Part I. General concepts, Revue Européenne des Eléments Finis 7 (5) (1998) 535–566.
[24] P.T. Sawbridge, E.C. Sykes, Dislocation glide in UO_2 single crystals at 1600°K, Philos. Mag. 24 (187) (1971) 33–53, doi:10.1080/14786437108216422.
[25] M. T. Hutchings, High-temperatures studies of UO_2 and tho_2 using neutron scattering techniques, J. Chem. Soc. Faraday Trans. 2 (89) (1987) 1083–1103.
[26] J. K. Engels, N. Vajragupta, A. Hartmaier, Parameterization of a non-local crystal plasticity model for tempered lath martensite using nanoindentation and inverse method, Front. Mater. 6 (2019) 247.
[27] J.A. Nelder, R. Mead, A simplex method for function minimization, Comput. J. 7 (1965) 308–313.

[28] C. Yust, C. McHargue, Dislocation substructures in deformed uranium dioxide single crystals, J. Nucl. Mater. 31 (2) (1969) 121–137, doi:10.1016/0022-3115(69)90187-1.
[29] B. Deng, A. Chernatynskiy, P. Shukla, S. Sinnott, S. Phillpot, Effects of edge dislocations on thermal transport in UO_2, J. Nucl. Mater. 434 (2013) 203–209.
[30] V. Baranov, A. Lunev, A. Tehishev, A. Khlunov, Interaction of dislocations in UO_2 during high burn-up structure formation, J. Nucl. Mater. 444 (2014) 129–137.
[31] M. R. G.Prasad, A. Biswas, K. Geenen, W. Amin, S. Gao, J. Lian, A. Röttger, N. Vajragupta, A. Hartmaier, Influence of pore characteristics on anisotropic mechanical behavior of laser powder bed fusion–manufactured metal by micromechanical modeling, Adv. Eng. Mater. 22 (12) (2020) 2000641.
[32] M. Lindroos, J.-M. Scherer, A. Laukkanen, T. Andersson, S. Forest, J. Vaara, A. Mantyla, T. Frondelius, Micromechanical strain gradient approach to plasticity and damage in martensitic steels, Int. J. Plast. 151 (2022) 103187.
[33] Z. Que, M. Lindroos, J. Lydman, N. Hytonen, S. Lindqvist, P. Efsing, P. Nevasmaa, P. Arffman, Brittle fracture initiation in decommissioned boiling water reactor pressure vessel head weld, J. Nucl. Mater. 569 (2022) 153925.